# Microtopographical guidance of macropinocytic signaling patches

Gen Honda[a] , Nen Saito[b,c], Taihei Fujimori[a], Hidenori Hashimura[a], Mitsuru J. Nakamura[a], Akihiko Nakajima[a,d], and Satoshi Sawai[a,b,d,e,1]

[a]Department of Basic Science, Graduate School of Arts and Sciences, University of Tokyo, Meguro-ku 153-8902, Japan; [b]Universal Biological Institute, University of Tokyo, Bunkyo-ku 113-0033, Japan; [c]Exploratory Research Center on Life and Living Systems, National Institutes of Natural Sciences, Okazaki 444-8787, Japan; [d]Research Center for Complex Systems Biology, University of Tokyo, Meguro-ku 153-8902, Japan; and [e]Department of Biology, Graduate School of Science, University of Tokyo, Bunkyo-ku 113-0033, Japan

In fast-moving cells such as amoeba and immune cells, dendritic actin filaments are spatiotemporally regulated to shape large-scale plasma membrane protrusions. Despite their importance in migration, as well as in particle and liquid ingestion, how their dynamics are affected by micrometer-scale features of the contact surface is still poorly understood. Here, through quantitative image analysis of *Dictyostelium* on microfabricated surfaces, we show that there is a distinct mode of topographical guidance directed by the macropinocytic membrane cup. Unlike other topographical guidance known to date that depends on nanometer-scale curvature sensing protein or stress fibers, the macropinocytic membrane cup is driven by the Ras/PI3K/F-actin signaling patch and its dependency on the micrometer-scale topographical features, namely PI3K/F-actin–independent accumulation of Ras-GTP at the convex curved surface, PI3K-dependent patch propagation along the convex edge, and its actomyosin-dependent constriction at the concave edge. Mathematical model simulations demonstrate that the topographically dependent initiation, in combination with the mutually defining patch patterning and the membrane deformation, gives rise to the topographical guidance. Our results suggest that the macropinocytic cup is a self-enclosing structure that can support liquid ingestion by default; however, in the presence of structured surfaces, it is directed to faithfully trace bent and bifurcating ridges for particle ingestion and cell guidance.

actin waves | macropinocytosis | topography | cell migration | contact guidance

Large-scale deformation of plasma membrane during cell migration, particle, and liquid ingestion depends on physical cues such as substrate rigidity and topography (1–4). Cell migration along ridges and grooves is generally referred to as contact guidance and thought to play pivotal roles in neural development (5), tissue repair, immune response, and cancer invasion (6). Topography-dependent cell movements known to date are associated with anisotropic contractility through alignment of stress fibers. Nano- and microfabricated platforms have clarified how geometrical constraint affects distribution of focal adhesions and actin stress fibers (7, 8). While such a mechanism appears to be widespread in cells of epithelial or mesenchymal nature (3, 9), topographical guidance in fast-moving amoeboid cells (10–13) which do not have stress fiber is far less understood. Neutrophils are known to elongate along grooves of a hemocytometer (10). T cells migrate along parallel ridges/grooves whose widths are hundreds of nanometers (11). Adhesion-independent mode of migration in T cells occurs under two-dimensional confinement only if there is topographical asymmetry in the physical surrounding (14). While there are large body of work addressing how diffusible chemoattractants determine when and where the leading edge forms, how they are guided by topography remains largely unknown.

The leading edge of migrating cells has a large overlap in its molecular compositions with that formed during particle and liquid ingestion and thus the distinction is often obscure (15). Conventionally, uptake of particles and liquid are referred to as phagocytosis and macropinocytosis, respectively. Both processes involve large-scale conversion from contractile actomyosin to protrusive branched actin meshworks, which generate force to expand a cup-shaped membrane invagination (16, 17). Phagocytosis occurs through the so-called "zippering mechanism" where the protruding edge of the cup is sequentially extended along the attached solid surface while forming an anchorage with the decorated opsonins [i.e., scaffold antigens or complements (18, 19)]. Macropinocytic cup formation, on the other hand, is a self-organizing process which does not require specific anchorage and traction to shape the membrane (18, 19). While this property makes it suitable for the uptake of nutrient media as well-studied in cancer cells and *Dictyostelium*, particle uptake is also known [e.g., entry of pathogenic bacteria into the host cells (20)]. Nonopsonized beads can be ingested by *Dictyostelium* as well as immune cells (21–23). The receptor-independent cues that guide these ingestive membrane protrusions are largely unknown.

Unlike the well-studied nanometer-scale endocytic cups (24–26), phagocytic and macropinocytic cups involve much larger (close to a cell length) scale reorganization of actin cytoskeletons. In *Dictyostelium*, phagocytic/macropinocytic cup

## Significance

Morphologies of amoebae and immune cells are highly deformable and dynamic, which facilitates migration in various terrains, as well as ingestion of extracellular solutes and particles. It remains largely unexplored whether and how the underlying membrane protrusions are triggered and guided by the geometry of the surface in contact. In this study, we show that in *Dictyostelium*, the precursor of a structure called macropinocytic cup, which has been thought to be a constitutive process for the uptake of extracellular fluid, is triggered by micrometer-scale surface features. Imaging analysis and computational simulations demonstrate how the topographical dependence of the self-organizing dynamics supports efficient guidance and capturing of the membrane protrusion and hence movement of an entire cell along such surface features.
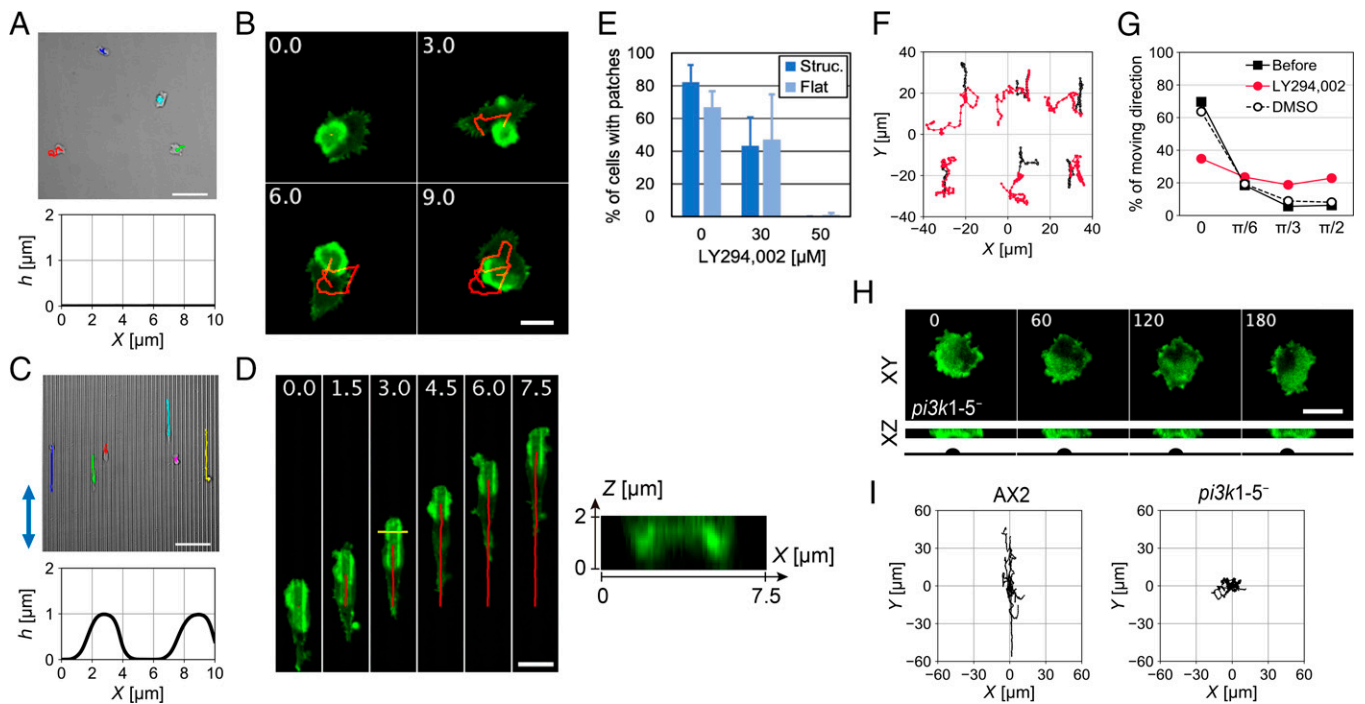
**Fig. 1.** The ventral actin patch travels along a micrometer-scale ridge and guides cell movement. (*A–D*) Cell trajectories and the ventral actin patch dynamics in aggregation-stage AX4 cells on flat (*A* and *B*) and structured SU-8 surface (*C* and *D*). (*A* and *C, Upper*) Transmitted-light images of a representative field of view. Colored lines: trajectories of individual cells for 20 min (Scale bars, 50 μm). (*A* and *C, Lower*) Representative surface geometry. (*B* and *D*) Time-lapse confocal images of the actin patch. Green: GFP-Lifeact; *z*-slice near the SU-8 surface (*z* = 0) (*B*), and maximum intensity projection (MIP) from *z* = 0 to 2 μm (*D, Left*) and the cross-section along the yellow line (*D, Right*). Red lines: centroid trajectories of the actin patch. Time in min (Scale bars, 10 μm). (*E*) Fraction of patch-positive cells after LY294,002 treatment (mean ± SE, >13 cells per condition). (*F*) Cell trajectories before (black, time duration 5 min) and after (red, time duration 13 min) LY294,002 application. (*G*) Angular distribution of cell displacement relative to the ridges before (black solid line; *n* = 14 cells) and after LY294,002 application (red line; *n* = 6 cells). DMSO mock control (black broken line; *n* = 8 cells). (*H*) GFP-Lifeact/ *pi3k1-5⁻* cell (MIP from *z* = 0 (near the substrate) to 2 μm on *XY*- (*Upper*) and *XZ* plane (*Lower*). Time in s (Scale bar, 10 μm). (*I*) Trajectories of patch(+) AX2 and *pi3k1-5⁻* cells (time duration 10 min; *n* = 11 and 13 cells) on the structured SU-8 surface.

formation begins with the appearance of micrometer-size patches enriched in dendritic actin filaments, whose inner domain has strong accumulation of phosphatidylinositol (3,4,5) trisphosphate (PIP3) (27) along with GTP-bound form of Ras and Rac. These active signaling patches are self-amplified by a positive-feedback loop involving Ras and PI3K (28–30) and serve as a common precursor or "template" for the cup formation (31, 32). As the patch increases in size, its outer edge enriched in the SCAR/WAVE complex protrudes outward to form a circular ruffle (32). Loss of RasGAP enhances both phagocytosis and macropinocytosis (33–35), indicating that Ras act positively on both processes. While deletion or pharmacological inhibition of PI3K suppresses liquid uptake, the deleterious effect on phagocytosis is limited to the uptake of large particles (27, 36, 37). The identical molecular organization is observed in the ventral side facing the substrate, where they appear as patches that travel as "waves" (29, 32, 38). The ventral patches are thought to be a frustrated form of a macropinocytic cup (31) akin to the frustrated phagosomes in macrophage (39). In this work, to clarify the relationship between the macropinocytic patch dynamics and the surface microscale topography, live-cell imaging analysis of *Dictyostelium* cells on microfabricated surfaces was performed. We demonstrate that the patch travels along a micrometer-scale ridge and supports surface capturing and cell guidance. Nucleation of the signaling patches at the level of Ras-GTP occurs at the convex surface independent of PI3K and F-actin. Guidance of patches requires PI3K-dependent membrane evagination, which is constricted at the concave surface in an actomyosin-dependent manner. Together with three-dimensional (3D) simulations of a mathematical model for

macropinocytic cup formation, our results indicate that the combined effects of topography-dependent initiation of the signaling patch and the cup forming dynamics serve as the basis of the topographical guidance

## Results

**The Ventral Patch Propagates along Micrometer-Scale Ridges and Directs *Dictyostelium* Cell Migration.** To gain an overview of the microtopography dependency, the aggregation-stage *Dictyostelium discoideum* cells (axenic strain AX4 expressing green fluorescent protein [GFP]-labeled Lifeact) were plated on a SU-8 substrate with or without parallel ridges (1 μm high, 3 μm wide, and 3-μm interval), and their behavior was compared by time-lapse confocal imaging. Cells were manually scored at each time frame for the presence of intense patches of F-actin on the ventral plasma membrane. On both flat and structured surfaces, the percentage of cells with one or more patch increased from 2 h after plating (*SI Appendix*, Fig. S1*A*) and reached 79 ± 13% and 98 ± 1% on flat and microstructured surfaces, respectively (*SI Appendix*, Fig. S1 *A, Right*, 250 min). On the flat surface, cells with the ventral patch (patch(+) cells) did not show directional movement (Fig. 1*A*). Its displacement oriented randomly [*SI Appendix*, Fig. S1*B*; patch(+)] and was small compared with cells without the patches [*SI Appendix*, Fig. S1*B*; patch(−)]. The direction of patch propagation also changed frequently (Fig. 1*B*; red trajectories, Movie S1). On the microstructured surface, patch(+) cells migrated along the ridge [Fig. 1*C* and *SI Appendix*, Fig. S1*C*; patch(+)] while the patch remained in its anterior (Fig. 1*D* and Movie S2), and their movement seldom deviated from a single track. The presence

of the patch was strongly correlated with the directed migration along the ridge (*SI Appendix*, Fig. S1*D*; 0 rad), while the speed of cell centroid was not largely affected (*SI Appendix*, Fig. S1*E*). The average directional persistence time in patch(+) cells increased from 0.54 min on the flat surface to 13.7 min on the structured surface [*SI Appendix*, Fig. S1*F*; Flat, (+), Struc, (+)]. In contrast, the persistence time was not affected in patch(−) cells; 3.0 min on the flat surface and 4.6 min on the structured surface [*SI Appendix*, Fig. S1*F*; Flat, (−), Struc, (−)].

The actin patch and the leading edge moved along a single ridge and rarely traversed to neighboring ridges. Some cells migrated in one direction for over 30 min before switching direction, while others frequently made turns and consequently showed small net displacement, less than 80 μm throughout our 50-min time-lapse observations (*SI Appendix*, Fig. S1*G*). Change in the migration direction was accompanied by either patch reversal or splitting (*SI Appendix*, Fig. S1 *H* and *I*). In reversal, the actin patch traveled from the cell anterior to the opposite end (*SI Appendix*, Fig. S1*H*). In splitting, the anterior patch separated in half, and a daughter patch reached the posterior end to become a new front while the other patch disappeared (*SI Appendix*, Fig. S1*I*). Cells that exhibited frequent patch reversal and splitting showed small net displacement (*SI Appendix*, Fig. S1*J*). In less-polarized growth-stage cells, almost the entire ventral side of the plasma membrane was covered by a single patch if not a few separate patches at most, resulting in large ruffles projected in many directions (*SI Appendix*, Fig. S2*A*, Flat). Here, small patches were restricted to the ridges (*SI Appendix*, Fig. S2*A*, Ridge, 24 to 48 s), while larger ones often covered several ridges (*SI Appendix*, Fig. S2*A*, Ridge, 72 to 120 s). In both patch(−) and patch(+) growth-stage cells, persistent migration along the ridge seldom occurred (*SI Appendix*, Fig. S2*B*; refer to *SI Appendix*, Fig. S2*C* for a rare case). These results indicate that microtopographical features guide patch propagation, which can also guide cell migration in differentiated cells.

**The Microtopography Guidance Is Mediated by Macropinocytic Signaling Patches and Is Incompatible with Chemotaxis.** These observations raise a question whether the macropinocytic signaling patch was replaced by some other process when presented with curved surfaces. Spatial organization of the key molecular components that define the ventral patch on flat surfaces (29, 32, 40) mapped well to the patch observed at the ridge [i.e., Ras-GTP, Rac-GTP, PI(3,4,5)PIP3, and Talin A at the inner domain and PI3K, SCAR complex, Talin B, and F-actin at the patch rim (*SI Appendix*, Fig. S3)]. The default membrane state that surrounds the patch was enriched in PTEN, Myosin II, and an actin crosslinker Cortexillin I (*SI Appendix*, Fig. S3), which is also consistent with the pattern observed on flat substrates (29, 40). These observations indicate that the membrane evagination surrounding the ridge is a large macropinocytic cup in a frustrated state. When assayed for the uptake of fluorescein isothiocyanate (FITC)-labeled dextran from the surrounding buffer (27, 34), cells on the structured substrate showed as much as 59.6% reduction (*SI Appendix*, Fig. S4*A*) compared with cells on the flat surface. A possible interpretation of this result is that the continued presence of a frustrated macropinocytic cup interferes with the dynamics from taking place elsewhere. Such a notion is supported by an earlier observation that when cells are sandwiched between two planes, the patch often appears on one side only (41).

Another good indicator of macropinocytic patch at least for cells in growth-stage or cells early into differentiation is that it can be extinguished by PI3kinase inhibitor LY294,002 (29, 30). We observed that in the aggregation-stage cells too and on the ridge, the patch was extinguished by LY294,002 treatment in a dose-dependent manner (Fig. 1*E*). When applied with LY294,002 using a microneedle, the patch disappeared, and the cell trajectories deviated from the ridge (Fig. 1*F*, red). Directional bias decreased to a level comparable to nontreated cells without the ventral patch [Fig. 1*G*, LY294,002, compare with *SI Appendix*, Fig. S1*D*; Struc., (−)]. A mock treatment with dimethyl sulfoxide (DMSO) had no effect on the patches and the guidance (Fig. 1*G*, DMSO). Although these results further support the causal relationship between the patch and topographical guidance, because LY294,002 is a broad-spectrum inhibitor (42), extinction of the patch may be due to inhibiting multiple kinases in addition to PI3K. In the PI3K-null (*pi3k1-5⁻*) cells, the patch was still observed at the level of F-actin, in agreement with recent reports (30, 32); however, they did not propagate along the ridge (Fig. 1*H*). Accordingly, in contrast to the parental axenic strain AX2, which showed clear directional migration along the ridge (Fig. 1 *I, Left*), *pi3k1-5⁻* cells showed random movement (Fig. 1 *I, Right*). F-actin accumulation at the rim of the patch was markedly reduced especially near the cell edge in *pi3k1-5⁻* compared with its parental AX2 (*SI Appendix*, Fig. S5 *A* and *B*), which is consistent with an earlier observation of weak SCAR complex localization in *pi3k1-5⁻* cells (32) and the positive-feedback regulation between PI3K and F-actin (28). These results indicate that while the appearance of the patch per se does not require PI3K, its guidance along the ridge is strictly PI3K dependent. The confinement of the patch appears not to depend on the strict turnover rate of phosphoinositides because while the speed of the patch propagation was slow for both *pi3k1-5⁻* and the null strain of 3′-phosphatase PTEN (*SI Appendix*, Fig. S5 *C–E*), the positional restriction to the ridge was intact in *pten⁻* cells (*SI Appendix*, Fig. S5*F*). We should also note that the observed topographical guidance is distinct from the earlier reported LY294,002-insensitive biased cell migration along submicrometer-scale ridges (13). Nanometer-scale–dependent processes are known to often involve SH3-domain–containing BAR protein (24, 26). Similar to mammalian cells, we found that SH3- and BAR domain–containing Nwk/Bzz1p-like protein (NLP) (43) exhibited membrane localization along the surface of polystyrene beads smaller than 1-μm radius but not larger (*SI Appendix*, Fig. S4 *B* and *C*). Accordingly, no clear colocalization of NLP with the patch was observed on the micrometer-scale ridge (*SI Appendix*, Fig. S3 *B* and *C*). Two other SH3-domain–containing BAR proteins, SLP and DDB_G0271812, were checked, and we did not detect localization adjacent to the beads (*SI Appendix*, Fig. S4 *B* and *C*). These results indicate that the macropinocytic signaling patch mediates distinct micrometer-scale topography guidance.

The high directedness of the topographically guided movements suggests potential crosstalk with chemotaxis. Cells exposed to a concentration gradient of cAMP formed from the tip of a glass needle exhibited two types of response (*SI Appendix*, Fig. S6 *A* and *B* and Movie S3). In approximately one-half of the case, actin patches disappeared within 5 min after stimulation [*SI Appendix*, Fig. S6*E*; 37.5% on the microstructured (*n* = 40 cells) and 58.5% on the flat (*n* = 41 cells)] surfaces, and the cells migrated up the gradient (*SI Appendix*, Fig. S6*A*). For the rest of the case, actin patches persisted, and cells continued to migrate along the ridge irrespective of the gradient orientation (*SI Appendix*, Fig. S6*B*). Cell trajectories on a flat (*SI Appendix*, Fig. S6*C*) and a structured (*SI Appendix*, Fig. S6*D*) substrate clearly show that chemotaxis was markedly suppressed when the actin patches were present. The mean migration speed toward the cAMP source was close to zero in patch-positive cells (*SI Appendix*, Fig. S6*F*). Erasure of patches by the cAMP stimulation was more pronounced and rapid in cells on the flat surface compared with those on the structured surface (*SI Appendix*, Fig. S6*E*). After 10 min, while the patches remained diminished in cells on the flat substrate, they were
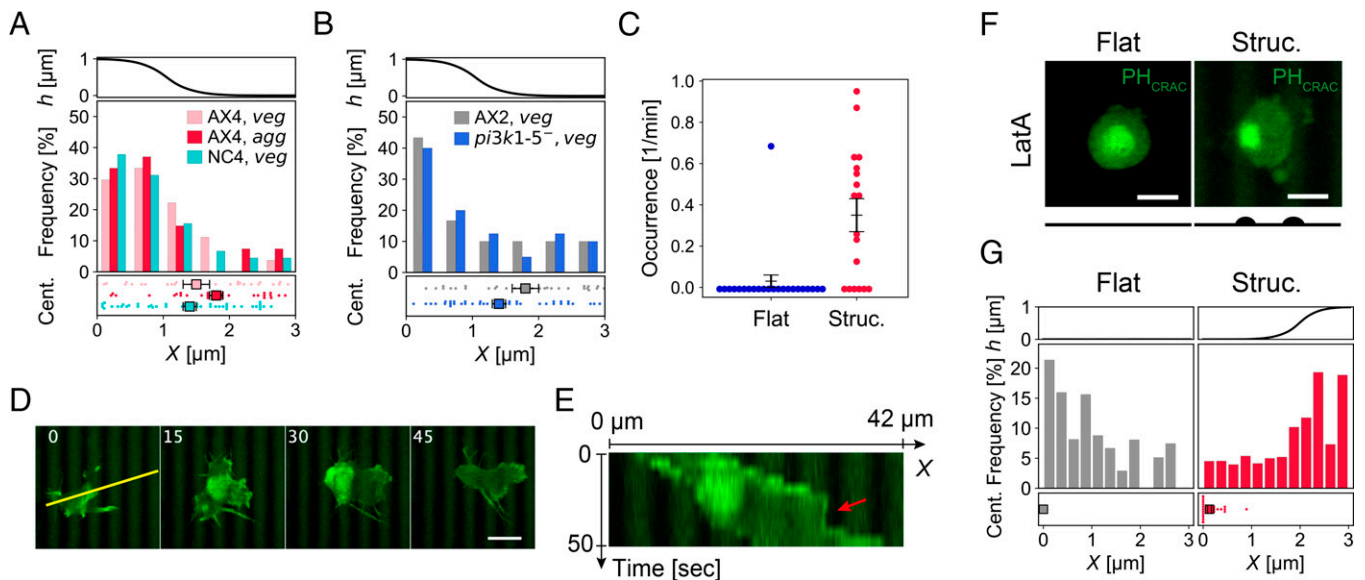
**Fig. 2.** Ras-GTP patch is preferentially initiated at the ridge independent of PI3K/F-actin. (*A* and *B*) Distribution of F-actin (*A*) and Ras-GTP (*B*) patch nucleation along the *x*-axis (*Upper*: the ridge *z*-profile) for (*A*) aggregation-stage (*agg*) AX4 cells, vegetative (*veg*) AX4 and NC4 cells, and (*B*) vegetative AX2 and *pi3k1-5⁻* cells (*Middle*). Cell position at the time of patch nucleation (*Bottom*, mean ± SE, *n* = 28 (AX4, *veg*), 27 (AX4, *agg*), 45 (NC4, *veg*), 30 (AX2, *veg*), and 40 patches (*pi3k1-5⁻*, *veg*), each dot represents a unique cell). (*C*) Frequency of ventral actin patch nucleation in vegetative NC4 cells [mean ± SE, *n* = 23 (Flat) and 18 cells (Structured), each dot presents a unique cell]. (*D*) Lifeact-GFP/NC4 on ridges (green: Lifeact-GFP; MIP from *z* = 0 to 3 μm). Time in s (Scale bar, 10 μm). (*E*) A kymograph along the yellow line in *D*. The image is enlarged eight times in time axis by pixel interpolation for visibility. (*F*) Representative snapshots from confocal images of vegetative NC4 cells expressing PH$_{CRAC}$-GFP that are treated with 3 μM LatA on flat (*Left*) and microstructured (*Right*) surfaces (green: PH$_{CRAC}$-GFP; MIP from *z* = 0 to 3 μm, the *Lower* schematic indicates ridge positions) (Scale bars, 5 μm). (*G*) Distribution of PH$_{CRAC}$ patch nucleation in LatA-treated NC4 cells; flat (*Left*, *n* = 75 patches) and structured (*Right*, *n* = 118 patches) surface (*Middle*). *x* = 0 is set to cell centroid for flat surface and the trough for structured surface (*Upper*: surface *z*-profile). Cell position at the time of patch nucleation (*Bottom*, mean ± SE, each dot represents a unique cell).

restored in cells on the structured substrate. The same cell was observed to switch between the two behaviors; cells that first migrated up a cAMP gradient (*SI Appendix*, Fig. S6 *G* and *H*, 0 to 100 s) stopped as a ventral actin patch appeared (*SI Appendix*, Fig. S6 *G* and *H*, 110 to 210 s), then again resumed chemotaxis as soon as the patch disappeared (*SI Appendix*, Fig. S6 *G* and *H*, 220 to 300 s). Small protrusions toward the cAMP source were observed in some cells during microtopographical guidance (*SI Appendix*, Fig. S6*I*), suggesting that patch(+) cells still responded to extracellular cAMP. These results indicate that chemoattractant stimulus suppresses patch formation; however, this effect is counteracted by the ridge structure.

**Signaling Patch Is Preferentially Initiated at the Ridge Independent of PI3K/F-actin.** The observation suggests that patch formation is promoted by microtopography. Measurements of the positions of patch nucleation relative to the surface topography show that majority of the ventral patches were initiated at the ridge in both growth- and aggregation-stage cells (Fig. 2*A*; AX4, *veg* and AX4, *agg*), independent of the position of the cell centroid (Fig. 2 *A*, *Bottom*). Note that because the analysis is per nucleation basis, many of the instances detected were during transients prior to or in between migration events along the ridge. The duration that a growth-stage cell had one or more patches was on average 244 ± 54 s (*n* = 20 events) and 654 ± 111 s (*n* = 24 events) on flat and structured surfaces, respectively. In aggregation-stage cells, majority of patches persisted throughout our time-lapse observations (50 min). Conversely, when the surface was coated with lectin wheat germ agglutinin, which enhances attachment of *Dictyostelium* cells (44), the occurrence of actin patches decreased markedly (*SI Appendix*, Fig. S7 *A* and *B*). The lifetime decreased to 4.0 ± 0.6 min (structured, *n* = 22 patches; flat, no patch), and the directional bias also diminished (*SI Appendix*, Fig. S7*C*, compare with *SI Appendix*,

Fig. S1*D*). The positional bias of the patch initiation was also observed in *pi3k1-5⁻* cells at the level of Ras-GTP (Fig. 2*B*), indicating that it does not require PI3K.

An earlier study suggested that the increased appearance of the signaling patches in the axenic strains is due to null mutation in RasGAP NF1 (32). Therefore, we tested the parental nonaxenic strain (NC4), which has the intact RasGAP. Growth-stage NC4 cells were analyzed because actin patches were absent in the aggregation stage. On a flat surface, only a few percent of the cells exhibited patches (4.3%, *n* = 23 cells) in agreement with an earlier study (32). In contrast, the percentage increased drastically on the structured substrate (67%, *n* = 18 cells). The occurrence of patches was 0.03 ± 0.03/min and 0.35 ± 0.08/min for flat and structured surfaces, respectively (Fig. 2*C*). Majority of the patches were initiated at the ridge (Fig. 2*A*, NC4, *veg*). These patches were relatively short lived (Flat, 34 ± 5 s, *n* = 8 patches; Struc., 21 ± 2 s, *n* = 42 patches) and did not facilitate migration; however, they competed with the leading-edge protrusion (Fig. 2*D*, *t* = 15 to 30 s, Fig. 2*E*; red arrow). Interestingly, in NC4 cells treated with actin polymerization inhibitor LatrunculinA (LatA), the patches of a PIP3 marker (PH$_{crac}$-GFP) appeared even on the flat surface (Fig. 2 *F*, *Left*) as well as on the structured surface (Fig. 2 *F*, *Right*) (Movie S4). Here too, there was a strong bias in the occurrence of the patch at the ridge (Fig. 2 *G*, *Right*). These patches remained at the site of initiation (*SI Appendix*, Fig. S8 *A*, *Right*) and disappeared spontaneously (Movie S4). The results indicate more stringent microtopography dependency of patch initiation in NC4 compared with the axenic strains. However, caution is needed in interpreting the results because LatA-treated cells tend to sink down and become trapped between two neighboring ridges due to immobility, so that the ridge inevitably coincides with the cell edge. On the flat surface, the patch initiation in LatA-treated cells was skewed rather
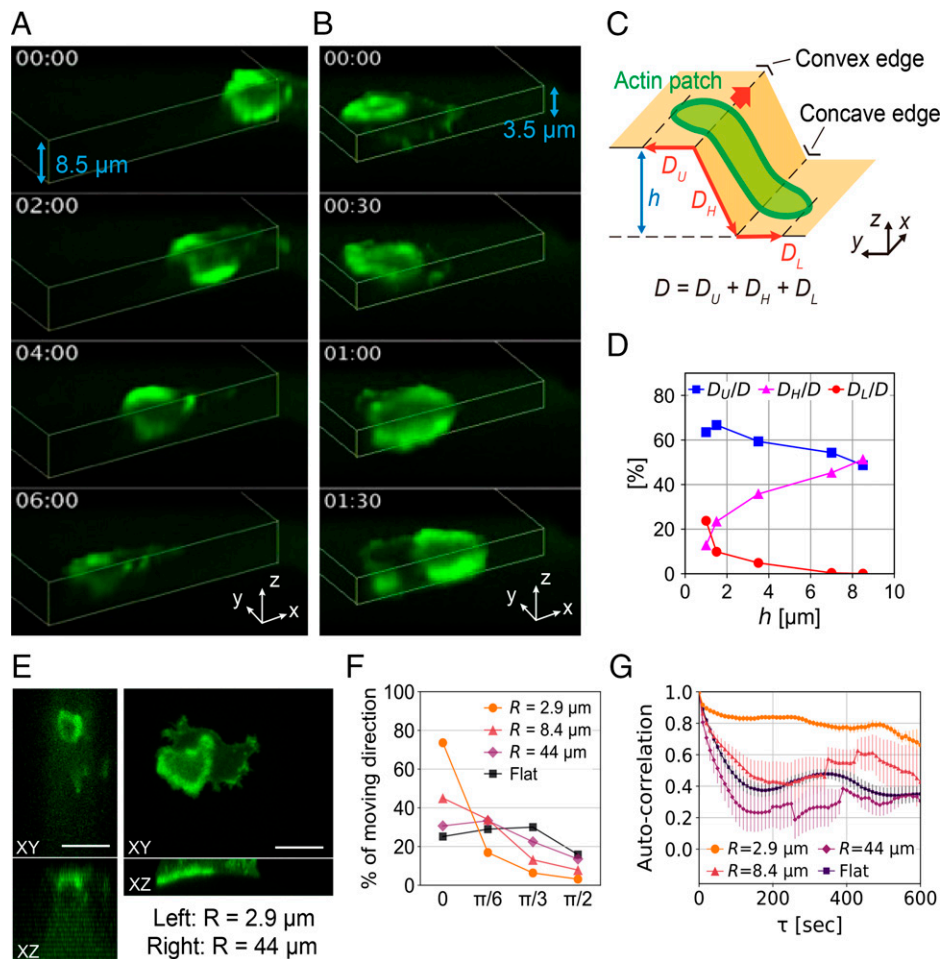
**Fig. 3.** Patch propagation is directed along the convex edge and stalled at the concave edge. (*A* and *B*) 3D time-lapse images of patch-positive cells on plateaus of 8.5 μm (*A*) and 3.5 μm (*B*) height (green: GFP-Lifeact; MIP in the direction 60 degrees from the *z*-axis, yellow: plateau contour). Time in min:s. (*C*) A schematic of parameters $D_U$, $D_H$, $D_L$, $D$, and $h$. (*D*) The height dependence of $D_U/D$, $D_H/D$, $D_L/D$ in AX4 cells. (*E–G*) Curvature dependence of patch propagation. (*E*) Patch-positive cells on triangular ridges with curvature radius $R = 2.9$ μm (*Left*) and $R = 44$ μm (*Right*) (green: GFP-Lifeact and SU-8 fluorescence; MIP from $z = 0$ to 20 μm ($R = 2.9$ μm) and $z = 0$ to 7 μm ($R = 44$ μm) into the *XY* (*Upper*) and *XZ* (*Lower*) plane) (Scale bar, 10 μm). (*F*) Angular distribution of centroid displacement of patch-positive cells relative to the ridge direction. (*G*) Autocorrelations of patch positions in the *XZ* plane (shown in *E*, *Lower*) on the ridges with various curvature (mean ± SE, $n = 4, 5, 5$, and 9 cells).

toward the center of the cell (Fig. 2 *G*, *Left*). Thus, while the intracellular positional bias cannot be ruled out in case of LatA-treated cells, the pattern is reversed and is thus overridden by the topography effect. The average fluorescence distribution of patches (*SI Appendix*, Fig. S8*B*), which measures where the patch tended to reside over time after its appearance, shows relatively small difference between the bottom ($X = 0$ μm) and the top ($X = 1.5$ μm) of the ridge in LatA-treated cells (*SI Appendix*, Fig. S8*B*, LatA) compared with untreated cells (*SI Appendix*, Fig. S8*B*, Untreated). This indicates that tight confinement of the patch to the ridge is facilitated by F-actin.

**Substrate Curvature Determines the Direction of Patch Propagation and Membrane Evagination.** In order to analyze the geometrical features that potentially constrain propagation of the signaling patch, we employed a SU-8 surface with a large plateau. On a plateau height ($h$) large enough to prevent a patch from covering both the top and bottom plane simultaneously ($h = 8.5$ μm), the patch propagated along the convex edge (Fig. 3*A*). On a low plateau ($h = 3.5$ μm), after traveling down from the top to the bottom (Fig. 3*B*, 00:00 ∼ 01:00), the patch changed direction and moved sideways along the ridge (Fig. 3*B*, 01:00 ∼ 01:30).

These observations suggest two opposing effects of the surface topography; convex surfaces attract and guide the patch, while concave surfaces prevent it from propagating further (*SI Appendix*, Fig. S9*A*). For more rigorous quantification, reconstructed 3D images were analyzed based on the spatial distribution of the patch with regard to the surface topography (Fig. 3*C*). Here, $D_U$ and $D_H$ are defined as the distances from the convex edge to the farthest points in a patch at the top and the lateral planes, respectively. $D_L$ is the distance from the concave edge to the farthest point in a patch at the bottom plane, and $D$ is the sum of $D_U$, $D_H$, and $D_L$. For patches observed on a high plateau ($h = 8.5$ μm), $D_U/D = 48 \pm 1\%$ and $D_H/D = 51 \pm 1\%$ (Fig. 3*D*, $n = 83$ plots), meaning that patches expanded equally well toward the top and lateral plane (*SI Appendix*, Fig. S9 *C*, *Upper*). At the intermediate height ($h = 3.5$ μm), $D_U/D$ increased to $59.4 \pm 0.9\%$ while $D_H/D$ decreased to $35.8 \pm 0.7\%$ and $D_L/D = 4.9 \pm 0.5\%$ (Fig. 3*D*, $n = 117$ plots). Here, $D_U/D > D_H/D$ with $D_L/D$ close to zero which indicates that the concave edge is inhibitory to patch propagation (*SI Appendix*, Fig. S9 *C*, *Middle*). For a low plateau $h = 1$ μm, $D_L/D$ increased to $23.8 \pm 0.6\%$ (Fig. 3*D*, $n = 407$ plots), reflecting the spread of the patch to the bottom plane (*SI Appendix*, Fig. S9 *C*, *Lower*).

Honda et al.
Microtopographical guidance of macropinocytic signaling patches

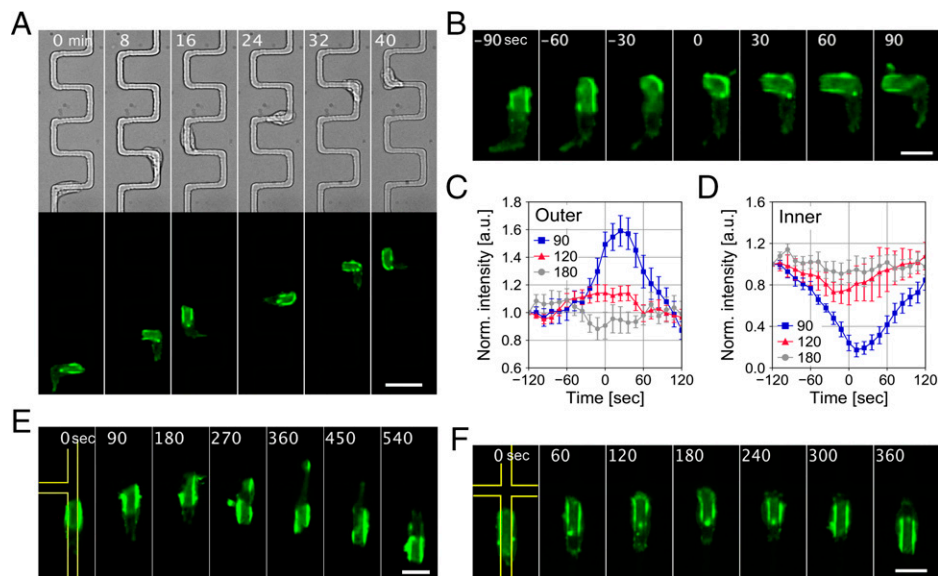PNAS | 5 of 11
https://doi.org/10.1073/pnas.2110281118

**Fig. 4.** Topographical dependence of patch propagation guides cells along zig-zag and bifurcating ridges. (*A* and *B*) Zig-zag ridges with 90-degree corners. (*A*, *Upper*) Transmitted-light images. (*A*, *Lower* and *B*) GFP-Lifeact; MIP from z = 0 to 2 μm. Zoom-up images of turning at the corner (*B*). (*C* and *D*) Change in the GFP-Lifeact intensity along the outer (*C*) and inner corners (*D*) with angles 90 (blue), 120 (red), and 180 (gray) degrees (mean ± SE, n = 16, 21, and 11 events). The patch centroid reached the corner at t = 0. (*E* and *F*) Patch reversal at a T-junction (*E*) and a X-junction (*F*). Yellow lines indicate the ridge contours. Time in min (*A*) and s (*B*, *E*, *F*) [Scale bars, 20 μm (*A*) and 10 μm (*B*, *E*, *F*)]. Ridge dimension: 1.5-μm height, 4-μm width.

At the concave edge, the rim of the patch is located at the interface of the dorsal and the ventral side of the plasma membrane (*SI Appendix*, Fig. S9A). In order for the patch to expand and form the protrusive actin networks, it must invade the region of the plasma membrane backed by crosslinked actomyosin (40). At the concave edge, actomyosin may be augmented locally to counteract expansion of the patch and the membrane protrusion. Indeed, when the patch stalled and became constricted to the ridge (*SI Appendix*, Fig. S9D, 40 to 80 s), there was accumulation of Myosin II at the dorsal side of membrane, and at the same time, the membrane was retracted to the side of the ridge (*SI Appendix*, Fig. S9E, 40 to 70 s). Myosin II accumulation weakened afterward (*SI Appendix*, Fig. S9E, 70 to 80 s) but stayed relatively high around the ridge on the dorsal side of the plasma membrane (*SI Appendix*, Fig. S3B, Myosin). Together with the near 90° contact angle against the bottom plane [*SI Appendix*, Fig. S3 *A*, *Lower* (asterisk) for the schematic], the results suggest high cell surface tension. Since crosslinkers of cortical actin (i.e., Myosin II and Cortexillin I/II) are essential for the cortical integrity and contractility in *Dictyostelium* (45, 46), we postulated that the patches in their null mutants may escape and travel across the concave edge. Indeed, in null mutants of Cortexillin I/II ($ctxI^-/ctxII^-$) and Myosin heavy chain A ($mhcA^-$), $D_L/D$ for h = 1.5 μm increased to 19 ± 1 and 25 ± 2%, respectively, from 9.9 ± 0.4% in AX4 (*SI Appendix*, Fig. S9F). Furthermore, patches in $mhcA^-$ and $ctxI^-/ctxII^-$ propagated along the ridge but was not confined ($mhcA^-$ in *SI Appendix*, Fig. S9G; $ctxI^-/ctxII^-$ in *SI Appendix*, Fig. S10C, 0 to 150, 750 s). Notably, in $mhcA^-$, patches often traversed between the ridge and the bottom plane (*SI Appendix*, Fig. S9 *H* and *I*). We should note that, based on the continued expansion of the circular F-actin rich domain (*SI Appendix*, Fig. S9G; *SI Appendix*, Fig. S10C, 750 s, asterisks), it is not just the membrane but also the signaling patch that is expanding to the bottom plane. These observations are compatible with the observation of LatA-treated cells (*SI Appendix*, Fig. S8B) and suggest that the cortical actomyosin at the dorsal side supports patch constriction at the concave edge.

To further address the geometry requirement of the convex edge, ridges of different curvatures were fabricated (*SI Appendix*, Fig. S9J). Here, the contour of the ridge was set larger than the average patch diameter ~10 μm so that a single patch would not encompass the convex and concave edges simultaneously. At curvature radius R = 2.9 μm (*SI Appendix*, Fig. S9 *J*, *a*), the patch still propagated along the ridge (Fig. 3 *E*, *Left*) and guided directional cell movement (Fig. 3*F*, R = 2.9 μm). On the other hand, at R = 44 μm (*SI Appendix*, Fig. S9 *J*, *c*), patches propagated without preferred direction (Fig. 3 *E*, *Right*; Fig. 3*F*, R = 44 μm), appearing identical to those on the flat surface (Fig. 3*F*, Flat). The patch position along the curved surface (*SI Appendix*, Fig. S9K) fluctuated little at R = 2.9 μm (Fig. 3*G*), indicating tight trapping at the convex edge. The effects of the surface geometry are further vindicated by using zig-zag–patterned ridges of various angles in the *x–y* plane, which facilitate fluorescence microscopy imaging. Under this configuration, at each given corner, there is a convex edge on one side and a concave edge on the other (*SI Appendix*, Fig. S9B). For ±90° corners (Fig. 4*A* and Movie S5), we found that the cell anterior and the actin patch faithfully traced the ridge. During turning, strong accumulation of F-actin continued along the outer corner (convex in the horizontal plane), while it diminished at the inner corner (concave in the horizontal plane) (Fig. 4*B*, −90 ~ −30 s) before it recovered as the leading edge exited the corner (Fig. 4*B*, 0 ~ 90 s). Fluorescence intensities of GFP-Lifeact increased transiently at the outer corner by 1.6-fold (Fig. 4*C*, 90°) and decreased to 0.2-fold at the inner corner (Fig. 4*D*, 90°). With corners set at ±120° angle, the intensity fluctuation was smaller (Fig. 4 *C* and *D*, 120°), indicating that corners with sharper angles induce larger shifts in the level of F-actin accumulation. We also tested the patch behavior on intersecting ridges that form a T- or X- junction (*SI Appendix*, Fig. S10A). On a T-junction, a patch that entered the junction from the bottom of the T encountered two 90° corners facing the opposite directions. The patch stalled at both sides and sometimes reversed its direction (17.2%, *SI Appendix*, Fig. S10 *A*, *a*, Reverse). When a patch and the cell anterior entered the junction from the top of the T, they

# A

Side view | Top view | Top view (cross section)



# B

Side view | Top view | Top view (cross section)



# C
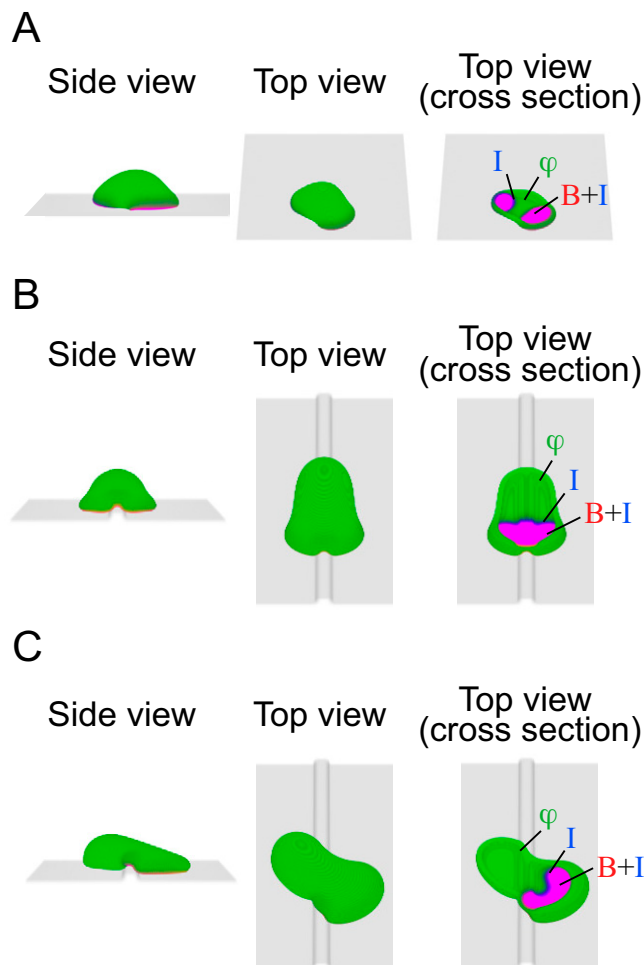
Side view | Top view | Top view (cross section)



**Fig. 5.** Three-dimensional simulations of the macropinocytic cup dynamics recapitulate the topographical guidance. (*A*–*C*) Representative snapshots from the simulations with a flat substrate (*A*) and with a ridge (height = 1.5 μm and width = 3.0 μm) (*B* and *C*). Surface tension was $\eta$ = 0.7 nN/μm (*A* and *B*) and 0.55 nN/μm (*C*). The signaling patch (red; $A_\psi > 0$), the inhibitor molecule (blue; $I_\psi > 0$) and the membrane (green; $\psi > 0$) [merged images; side view (*Left*), birds-eye view (*Middle*), and the cross-section along the plane parallel to the surface (*Right*)]. Other parameters are: $dx$ = 0.2 μm, $dt$ = $2 \times 10^{-4}$ s, $\varepsilon$ = 1.2 μm, $M_V$ = 5.0 nN/μm⁵, $\tau$ = 10.0 nN· s/μm³, $F$ = 2.6 nN/μm², $\beta$ = 100.0, $\theta$ = 0.105, $k_1$ = 0.05 s⁻¹, $k_2$ = 0.5 s⁻¹, $a_t$ = 1.6, $D_a$ = 0.17 μm²/s, $D_i$ = 0.13 μm²/s for (*A*) and $D_i$ = 0.1 μm²/s for (*B* and *C*), $K_1$ = 0.05, and $K_2$ = 0.04.

continued to propagate at the straight side while stalling at the concave side (Fig. 4*E*). The percentage of the patch that reversed its direction was 15.5% (*SI Appendix*, Fig. S10 *A, b*, Reverse). On X-junctions, which also have concave corners at both sides (Fig. 4*F* and Movie S6), patches also stalled at the intersection (Fig. 4*F*, 0 to 180 s), then reversed direction (Fig. 4*F*, 180 to 360 s; 27.6%, *SI Appendix*, Fig. S10 *A, c*, Reverse). These results further vindicate that the concave surface suppresses propagation of actin patches.

**Competition between Split Patches Depends on the Patch Size.** To study dependence of the patch behavior at the junction on Cortexillin, we employed Y-junctions (*SI Appendix*, Fig. S10*C* and Movies S7 and S8) since its threefold symmetry made data sampling efficient for systematic quantification. Here, turning to the left or right direction along the ridge occupied close percentages in the three strains tested: AX4, *ctxI⁻*, and *ctxI⁻/ctxII⁻* (*SI Appendix*, Fig. S10*B*, Turns), while reversal was never observed for *ctxI⁻* and *ctxI⁻/ctxII⁻* (*SI Appendix*, Fig. S10*B*,

Reverse). Splitting accounted for the rest of the percentage [i.e., 40.0% in AX4, 86.0% in *ctxI⁻*, and 75.4% in *ctxI⁻/ctxII⁻* (*SI Appendix*, Fig. S10*B*, Split)]. Here, the patch split into two, the cell was stretched in two opposing directions until one of the patches disappeared, and the surviving patch continued to guide the cells (Movies S7 and S8). To gain further insights, the time evolution of the patch size and the cell length along the ridge were analyzed (*SI Appendix*, Fig. S10 *E–G*). In all three strains tested, patch splitting was asymmetric in size, and the larger patch survived in most cases (*SI Appendix*, Fig. S10*F*). The maximal distance from the junction to the bifurcating cell edge (*SI Appendix*, Fig. S10*C*, $t$ = 600, *Inset*) for the surviving patch, $l_{s,\ MAX}$ was always larger than that of the diminishing patch $l_{d,\ MAX}$ (*SI Appendix*, Fig. S10 *G and H*). These results indicate the patch size at the time of splitting determines which of the bifurcating ridges is selected for the topography guidance.

There were a few observations worth noting in the Cortexillin-null mutants. Almost the entire ventral side of the plasma membrane was covered by the patch in these mutants [i.e., the patch leaked out from the ridge and the membrane spread out to the bottom plane (*SI Appendix*, Fig. S10*C*, 0 to 150 s)]. During splitting, the two fronts stretched out in the opposing directions and became more tightly constrained to the ridge (*SI Appendix*, Fig. S10*C*, 300 to 450 s), while the remaining stretched region that bridged the two branches was now not occupied by the patch (*SI Appendix*, Fig. S10*C*, 450 to 600 s, red arrows). Both $l_{s,\ MAX}$ and $l_{d,\ MAX}$ were longer in *ctxI⁻* and *ctxI⁻/ctxII⁻* compared with AX4 (*SI Appendix*, Fig. S10*H*). The magnitude of elongation ($l_{s,\ MAX} + l_{d,\ MAX}$) relative to the front-to-back cell length just before entering the junction ($l_0$) was 1. 29 ± 0.08, 1.59 ± 0.09, and 2.3 ± 0.1 for AX4, *ctxI⁻*, and *ctxI⁻/ctxII⁻*, respectively, which indicates that the patches move further apart in the *ctxI⁻* and *ctxI⁻/ctxII⁻* cells. The expansion slowed down and halted as one of the competing patches shrunk (*SI Appendix*, Fig. S10*D*, 340 to 600 s), and the membrane was retracted toward the surviving end (*SI Appendix*, Fig. S10*C*, 600 to 750 s). Interestingly, the surviving patch spread out from the ridge again to the bottom plane as soon as the patch disappeared on the other side (*SI Appendix*, Fig. S10*C*, 750 s, asterisks). More quantitatively, in AX4, the cell area outside the ridge in the splitting patches normalized to that in the nonsplitting patches was $A_S/A_{NS}$ 1.06 ± 0.04 in AX4 (*SI Appendix*, Fig. S10 *I and J*), meaning that the cell remained elongated tightly along the ridge. In *ctxI⁻* and *ctxI⁻/ctxII⁻*, $A_S/A_{NS}$ = 0.68 ± 0.04 and 0.71 ± 0.04, respectively (*SI Appendix*, Fig. S10 *I and J*), reflecting decrease in the membrane area that spread outside the ridge during stretching. These results suggest that the poor constriction of the patch to the ridge in *ctxI⁻* and *ctxI⁻/ctxII⁻* cells can be circumvented by the forward patch expansion and the accompanied stretching of the entire cell.

**A Reaction–Diffusion–Based Model of Macropinocytic Cup Formation Recapitulates Topography-Guided Cell Migration.** To see the relationship between the cup forming dynamics and the topographical guidance, we studied the outcome of a mathematical model of macropinocytic cup formation (47) when interfaced with a solid surface. The model describes a reaction–diffusion process that forms signaling patches on a deformable membrane. A patch can grow until it reaches a certain size limit. Based on the Arp2/3 localization and its alignment (48, 49), the model assumes that protruding force perpendicular to the membrane is restricted to the patch rim. 3D numerical simulations show that on both flat and structured surfaces the patch was confined to the ventral side as observed in the experiments (Fig. 5 *A* and *B*). On a flat surface, cups could not form due to large load by the physical barrier (Fig. 5*A* and Movie S9, *Left* panel). Whereas on a structured substrate with a linear ridge,

Honda et al.
Microtopographical guidance of macropinocytic signaling patches

PNAS | **7 of 11**
https://doi.org/10.1073/pnas.2110281118

protrusions were released from the frustrated state, and the resulting membrane extension covered the ridge (Fig. 5*B* and Movie S9, *Middle* panel). These behaviors stand in contrast to simulations of suspended cells where a patch expanded freely to form a self-enclosing cup structure (47). Interestingly, as the patch extends the membrane along the ridge, the direction of the patch propagation was naturally biased in the same direction (Fig. 5*B*). This behavior results from the very fact that patch dynamics and the membrane protrusion are mutually defining; a patch determines where the protrusive force is exerted, and the resulting membrane expansion defines where the patch would further occupy. Under reduced tension, the membrane spreads across the substrate, which further allows the patch to propagate outside the ridge (Fig. 5*C* and Movie S9, *Right* panel), which is in line with the behavior of the *mhcA*-null cells (*SI Appendix*, Fig. S9 *G* and *H*). The other essential requirement was that a small seed for the patch initiation had to be set at the ridge as an initial condition so that the membrane extension would be less hindered by the concave edge of the ridge. These results demonstrate that the topographical-dependent nucleation of the patch as observed at the level of Ras-GTP in PI3K-null cells provides the essential initial condition, which is then amplified into an expanding patch that can define the necessary force profile suited to guide the patch and the membrane according to topographical features.

## Discussion

Previous works suggested that the signaling patches of Ras/PIP3 in *Dictyostelium* are constitutive processes that serve as templates for phagocytic/macropinocytic cups (31, 32). The present work demonstrated that the signaling patch and the cup dynamics are topography dependent and serves to steer membrane protrusions along micrometer-scale structures. The topographical guidance consisted of 1) PI3K/F-actin–independent Ras-GTP patch initiation that is selective to convex surfaces of micrometer scale, 2) PI3K-dependent guidance of the patch and the membrane extension along the convex surface, and 3) actomyosin-dependent patch constriction at the concave surface. The topography-dependent patch nucleation and the ridge capturing suggest a mechanism whereby a cup is selectively generated when the plasma membrane is in contact with a sufficiently curved surface. We demonstrated that patch nucleation at the ridge is independent of PI3K (Fig. 2*B*) and F-actin (Fig. 2 *F* and *G*). Strict topographical dependence was observed in the wild-type NC4 strain (Fig. 2 *A* and *C*). Even for the axenic strain, which has hyper Ras activity and constitutive patch formation on flat surfaces (32, 33), our results demonstrate that the patch is preferentially initiated at the ridge (Fig. 2*A*), suggesting that topographical sensing still operates on top of the elevated Ras activity. Since forced elevation of Ras/Rap activity can enhance spontaneous patch generation (50), the present analysis indicates that surface topography has a similar effect on Ras but acting locally. Under chemoattractant stimulus, Ras is thought to be under adaptive feedforward-type regulation. Here, activation of RasGAP follows that of RasGEF, and both stay elevated so that the level of Ras-GTP is adjusted close to a fixed level (51, 52). Suppression of the patch by extracellular cAMP can be explained if one assumes RasGEF is activated or RasGAP is inhibited by the topography however weakly, so that it is canceled by the adaptive response elicited by the cAMP stimulus. Although the observed cell–cell variability in the preference between chemotaxis versus topography guidance may be associated with variability in these responses, it is unclear how they should be mutually exclusive. Strengthening the contact between the substrate and the plasma membrane also almost completely abolished the patch both on the flat and structured surfaces (*SI Appendix*, Fig. S7*B*). Because strong adhesion flattens the membrane, patch induction may be based on spontaneous curvature of lipid- and membrane-bound molecules (53). Alternatively, strongly adhesive conditions may be more directly inhibitory to patch initiation, propagation, or both. In several mammalian cell lines, ventral F-actin waves require a cycle of integrin engagement and disengagement to extracellular matrix (ECM) (54). We found that Talin A and Paxillin B localized to the inner region of the patch and Talin B to the rim where F-actin is enriched (*SI Appendix*, Figs. S3 *B* and *C* and S11 *A*–*C*). A potential role of Talin in Rap1 and PI3K signaling (55, 56) suggests that spatiotemporally coordinated turnover of cell–substrate adhesion may also be part of the patch dynamics.

According to our mathematical model, a self-enclosing membrane cup arises from size-limited patch expansion whose rim defines the position of the protrusive force (47). The model simulations indicate that as long as the initial seed of patch formation is given near the top of a ridge, membrane protrusion can push toward the indentation and enclose the ridge (Fig. 5*B*). According to this generic mechanism, the primary roles of PI3K are to restrict the protrusive force to the patch rim by mediating amplification of F-actin therein and to support patch propagation. While the former is simplified in the model by assuming a static force profile function (figure 1E in ref. 47), the process is likely more self-regulatory and involves feedback amplification of Ras, PI3K, and F-actin (30). Such notions are supported by the fact that, in *pi3k1-5⁻*, the patch is not constrained to the ridge (Fig. 1*H*), and F-actin at the rim is diminished (*SI Appendix*, Fig. S5 *A* and *B*). On the other hand, the elongated cell shape that closely covers the ridge can be explained by minimization of the cell surface area in addition to capturing of the ridge by the protruding membrane at the rim of the patch. In the model, under reduced surface tension, the membrane spreads beyond the concave edge and can hence allow the patch to escape (Fig. 5*C*). Poor confinement of the patch to the ridge in Myosin-null (*SI Appendix*, Fig. S9 *G*–*I*) and Cortexillin-null cells (*SI Appendix*, Fig. S10*C*) is consistent with their reduced cell surface tension (45, 46). A noticeable discrepancy likely due to oversimplification of the model, however, is that even when the patch was guided by the ridge, the patch and the membrane were not as well confined to the ridge in the simulation compared with the real cells (Figs. 1*D* and 5*B*). If topography dependence of Ras activity continues to hold during feedback amplification through PI3K/F-actin, such a property may support much tighter patch propagation along the concave edge. In addition, membrane translocation of Myosin II, Cortexillin I/II, and PTEN are known to be invoked by aspiration (57, 58) and thus mechanically regulated, and this can also reduce Ras-GTP (59). Such mechanochemical regulation may explain why trapping was temporarily improved in Cortexillin-null cells when being stretched at the bifurcating ridges (*SI Appendix*, Fig. S10 *I* and *J*). Absence of patch reversal at the junction in Cortexillin-null strains (*SI Appendix*, Fig. S10*B*) suggests that cortical contractility acts negatively on the patch persistence at the cell anterior also. Another important aspect is the speed of patch propagation which should be comparable to cell movement for it to effectively guide the cell. According to our model, without the inhibitor the reaction–diffusion scheme is no longer excitable and thus patch stalls (45). Given the fact that the patch propagation speed was significantly reduced in *pi3k1-5⁻* and *pten⁻* cells (*SI Appendix*, Fig. S5*C*), the activity of this hypothetical inhibitor may depend on the specific balance of phosphoinositides present in the plasma membrane.

All in all, our results suggest that PI3K play roles in guiding the patch along the convex feature, while Myosin II and Cortexillin I/II facilitates tight constriction of the patch toward the concave edge. These processes run in a self-regulatory manner

with the accompanying membrane protrusion and retraction. The topographical dependency is in line with earlier observations of trapping of actin patches at the sidewall of perforated microwells (60) and stalling of the cup at the furrow of a budding yeast (2). Such regulation may be a widespread mechanism for large particle uptake. In PI3K-null cells, the ingestion rate is severely impaired for yeast particles of 3 to 5 μm in diameter (36) but not for bacteria or 1-μm latex beads (27). Phagocytic uptake of IgG-coated beads in RAW264.7 cells requires PI3K when beads are larger than 3 μm in diameter (61). In macrophage, phagocytic cups are accompanied by Myosin II accumulation when tight contact is formed with IgG-opsonized erythrocytes (62). It should be noted that the macropinocytic signaling patches described here take place in the order of minutes, which contrasts with the nano-scale curvature-dependent waves of endocytosis that propagates in seconds timescale (63, 64). The distinction was also clear from the fact that a BAR domain protein that localized to submicrometer bead did not colocalize to the patch (*SI Appendix*, Figs. S3 *B* and *C* and S4 *B* and *C*). The macropinocytic guidance is also distinct from those based on mature focal adhesions (65) and actin cables (66, 67), which are both absent in *Dictyostelium*.

F-actin waves appear in the leading edge of migrating neutrophils (68) as well as in neuronal extensions during the neurite outgrowth (69); however, their role in *Dictyostelium* migration (50, 70) has been questioned due to its incompatibility with chemotaxis (71). Our work demonstrated a clear example of F-actin wave–directed migration. It was guided not by chemoattractant but by the substrate topography. Because NC4 cells did not exhibit this behavior, its migratory role is not clear. This puzzle parallels that for large-scale macropinocytosis in *Dictyostelium* as extracellular environment that supports it is also unknown (72). We envisage that the natural habitat that supports efficient macropinocytosis (i.e., large patch formation in nonaxenic wild-type is also likely to support "phagotactic" behavior). We note that vertically confined *Dictyostelium* formed phagocytic cup sideways facing a yeast particle in contact (*SI Appendix*, Fig. S12*A*). The cup which was more persistent in the aggregation-stage cells (*SI Appendix*, Fig. S12*B*) supported directed migration as the cell pushed the particle forward. Such movements may help cells transfer target particles to an open location for ingestion. Similar mechanisms may underlie streaming migration of macrophages in contact with target cancer cells (73) as well as during collective cell migration in *Dicyostelium* morphogenesis (74).

## Materials and Methods

**Surface Fabrication.** Microstructured SU-8 surfaces were prepared by standard photolithography. The structured surface used for cell assay consisted of two layers of fabricated SU-8 to make the surface homogeneous for cell attachment. Ridges with various curvature were fabricated by grayscale lithography. For construction of microgrooved glass substrates, glass coverslips (MATSU-NAMI, 0.13 ~ 0.17 mm in thickness) were loaded into a dry-etching system and etched by gas plasma. Microfabricated SU-8 and glass surfaces were measured using AFM (Nanowizard3, JPK, now Bruker) or DektakXT (Bruker). For precise estimation of the surface curvature, the substrate was coated by Cyanine5 fluorescence, and confocal Z-stack images were obtained. Refer to *SI Appendix, Materials and Methods* for details.

**Cell Preparation and Time-Lapse Imaging.** All plasmids and cell strains used in this study are described in *SI Appendix, Materials and Methods*. Axenic strains of *D. discoideum* were grown while shaken at 22 °C in HL5 with 60 μg/mL hygromycin B, 10 μg/mL G418 where appropriate. GFP-RBD$_{Raf1}$/*pi3k1-5$^-$* cells were cultured in HL5 supplemented with developmental buffer (DB) including *Escherichia coli* B/r at a final concentration OD$_{600}$ = 0.3 and then cultured in axenic medium for at least 2 d before assay. Lifeact-GFP/NC4 and PH$_{CRAC}$-GFP/ NC4 cells were cultured in DB including *E. coli* B/r at OD$_{600}$ = 6. For live-cell imaging, growing *Dictyostelium* cells were washed twice, resuspended in DB at 5 × 10$^6$ cells/mL and shaken at 22 °C, 155 rpm for 1 h. Cells were then pulsed with cAMP (final concentration 50 nM) every 6 min for 4.5 h. Starved cells

were plated at ~3 × 10$^3$ cells/cm$^2$ on a fabricated SU-8 or glass surface. For observation on glass surfaces (*SI Appendix*, Fig. S3), adenylyl cyclase inhibitor SQ22536 (Wako) was added at a concentration of 150 μM to circumvent cell–cell agglutination facilitated by the low adhesiveness of the glass surface. NC4 cells were collected by suspending in DB, pelleted by centrifuged at 100 × g for 3 min and resuspended in DB. The step was repeated three times to remove bacteria. Washed cells were plated at a density of ~1 × 10$^5$ cells/cm$^2$. For observation with yeast, AX2 cells expressing Lifeact-neon and yeast *Rhodotorula mucilaginosa* (NBRP, S90641) were loaded into polydimethylsiloxane chamber. The chamber was fabricated as previously described (75). Images were obtained using an inverted microscope (IX83 or IX81, Olympus) equipped with a laser confocal scanning unit (CSU-W1 or CSU-X1, Yokogawa) and an electron magnified CCD camera. For cAMP and LY-loading, 20 μL 100 nM cAMP and 100 μg/mL Alexa594 or 1 mM LY294,002 and 10 μg/mL Alexa594 were prepared in DB and loaded into Femtotips II (Eppendorf). The tip mounted on the micromanipulator (TransferMan 4r or TransferMan NK2, Eppendorf) was pressurized at 80 to 100 hPa using a microinjector (IM300, Narishige or FemtoJet, Eppendorf). All live-cell imaging was performed at 22 °C.

**Data Analysis.** Image analysis was performed using ImageJ, Python, and Microsoft Excel. To quantitate the relationship between cell migration and the ventral actin patches, confocal and transmitted-light images of GFP-Lifeact–expressing cells that were acquired using 20× objective lens at 1-min intervals for 50-min time windows (*n* = 6) were analyzed. To calculate the ratio of patch-positive cells, cells were manually assigned 1 or 0 according to the presence or the absence of the actin patches at each timepoint and averaged over all timepoints and cells (*SI Appendix*, Fig. S1*A*). Cell trajectories were obtained by auto or manual tracking of cell centroids (*SI Appendix*, Fig. S1 *B* and *C*). The average speed and distribution of migratory direction relative to the ridge were calculated from the centroid displacement in moving time window of 1 min (*SI Appendix*, Fig. S1 *D* and *E*). The relationship between the mean square displacement and time was fitted to the persistent random walk model (76) to obtain the persistence time (*SI Appendix*, Fig. S1*F*).

To measure the liquid uptake in cells adhered to the SU-8 surface (*SI Appendix*, Fig. S4*A*), FITC-dextran (Sigma, 46945-100MG-F, 70 kDa) solution was added to the surrounding buffer at a final concentration 0.5 mg/mL 3 h after plating the cells. 3D confocal images were acquired at 0, 1, and 2 h after adding FITC-dextran, and the number of fluorescent foci in the cytoplasm was counted. To evaluate the effect of LY294,002 treatment on patch formation (Fig. 1*E*), the average percentage of patch-positive cells in the same field of view was compared for 15-min time windows before (*t* = −15 to 0 min) and after (*t* = 10 to 25 min) application of the inhibitor (*t* = 0 min). The measurement was taken from several field of views in two independent trials per experimental condition. For quantification of spatial distribution of ventral PIP3 patches in Latrunculin A–treated cells (Fig. 2*G* and *SI Appendix*, Fig. S8*A*), 3D confocal images of PH$_{CRAC}$-GFP–expressing cells were acquired every 10 s for >5 min from *z* = 0 (the basal surface) to 3 μm at 0.5-μm interval. The distribution of the patch nucleation (Fig. 2*G*) was obtained based on the distance between the cell centroid and the patch along the *x*-axis (i.e., perpendicular to the ridge direction). The counts in histograms were corrected for the area of each bin and normalized against the total counts for all bins. To obtain the average spatial profile of PH$_{CRAC}$ (*SI Appendix*, Fig. S8*A*), the binarized mask of PH$_{CRAC}$-GFP patches and the cell outlines were extracted from the maximum intensity projection of Z-stacks and aligned against the average cell centroid positions. The aligned binary image stacks of patches and cell outlines were cropped to 180 × 90 pixels and averaged over 892 frames from 15 cells (Struc.) and 826 frames from 14 cells (Flat). The frequency of patches was normalized against the total value for all pixels. Averaged cell outlines were calculated in the polar coordinate system.

To measure localization of BAR domain–containing protein (*SI Appendix*, Fig. S4 *B* and *C*), cells were first starved and pulsed with cAMP for 4.5 h and suspended in DB at 1 × 10$^5$ cells/mL Fluorescent polystyrene beads (Invitrogen, φ0.2 μm, F8810, ×1/1,000 dilution and φ1.0 μm, F8821, ×1/100; Spherotech, φ2.0 μm, FP-2062-2, ×1/10 and φ6.0 μm, FP-6058-2, ×1/1) suspension was briefly vortexed and added to the cell suspension together with adenylyl cyclase inhibitor SQ22536 (Wako) at 200 μM (final concentration) and plated in a glass-bottom 24-well dish. Cells were allowed to settle for 30 min before measurement. Time-lapse confocal images were obtained every 10 s, and the time when BAR protein was membrane localized was counted by manually detecting strong puncta of GFP-tagged BAR protein near the bead surface. Detected time was divided by the total time the bead was in contact with the cell.

To quantitate the height dependence of patch dynamics on the plateau (Fig. 3*D*), Z-stacked time-lapse confocal images of cells expressing GFP-Lifeact

Honda et al.
Microtopographical guidance of macropinocytic signaling patches

PNAS | 9 of 11
https://doi.org/10.1073/pnas.2110281118

were acquired every 10 s. Images were projected into the *x*-axis in Fig. 3*C* as maximum fluorescent intensity were displayed. In the projected images, $D_U$, $D_H$, lengths from convex corner to the patch edges within top and lateral surfaces, $D_L$, a length from concave corner to the patch edge within bottom surface, and $D$, the sum of these three lengths, were measured at each timepoint. Ratio $D_U/D$, $D_H/D$, and $D_L/D$ were averaged over all timepoints from all cells and plotted. To quantitate the patch dynamics on the ridge with various curvature at its apex (Fig. 3*G* and *SI Appendix*, Fig. S9*J*), time-lapse Z-stacked confocal images of GFP-Lifeact were acquired every 10 s The region of actin patches were extracted from images of XZ plane projection and binarized. Kymographs of the patch presence were obtained by taking the binarized mask image of the patch along the curved surface. The contour length was normalized for comparison of autocorrelation in Fig. 3*G*.

For quantification of the relationship between the angle of the ridge corners and F-actin accumulation (Fig. 4 *C* and *D*), Z-stacked time-lapse confocal images of GFP-Lifeact–expressing cells plated on the zig-zag ridges were acquired every 6 or 12 s. From kymographs of GFP-Lifeact along the inner and outer corners, fluorescent intensities within actin patch regions were extracted and integrated at each timepoint. Time frame was aligned so that patch centroids reached the corner (Fig. 4*B*) at time 0. The integrated fluorescence intensities were normalized to the value at $t = -120$ s and averaged over all events. The membrane extension accompanied by two separate patches and the patch diameters on the Y-shaped ridges were quantitated using kymographs along both branches (*SI Appendix*, Fig. S10 *C–G*). Lengths from junction point to the two leading edges were defined as $l_s$ and $l_d$ (*s*: survived and *d*: disappeared). Cell area outside the ridge (*SI Appendix*, Fig. S10 *I* and *J*) was measured using binary cell-mask images created from GFP-Lifeact or Lifeact-neon fluorescence images from which the region of ridges were subtracted. The remaining area was time-averaged according to whether cells exhibited a single patch ($A_{NS}$) or two separate patches ($A_S$).

**Phase-Field Model.** Mathematical modeling and simulations were performed according to ref. 47. For details, refer to *SI Appendix, Materials and Methods*.

**Data Availability.** All study data are publicly available at RIKEN Systems Science Biological Dynamics (SSBD) database repository (https://ssbd.riken.jp/repository/182/).

1. J. A. Champion, S. Mitragotri, Role of target geometry in phagocytosis. *Proc. Natl. Acad. Sci. U.S.A.* **103**, 4930–4934 (2006).
2. M. Clarke *et al.*, Curvature recognition and force generation in phagocytosis. *BMC Biol.* **8**, 154 (2010).
3. A. Ray *et al.*, Anisotropic forces from spatially constrained focal adhesions mediate contact guidance directed cell migration. *Nat. Commun.* **8**, 14923 (2017).
4. D.-H. Kim *et al.*, Mechanosensitivity of fibroblast cell shape and movement to anisotropic substratum topography gradients. *Biomaterials* **30**, 5433–5444 (2009).
5. G. Reig, E. Pulgar, M. L. Concha, Cell migration: From tissue culture to embryos. *Development* **141**, 1999–2013 (2014).
6. P. Friedl, S. Alexander, Cancer invasion and the microenvironment: Plasticity and reciprocity. *Cell* **147**, 992–1009 (2011).
7. C. Oakley, D. M. Brunette, The sequence of alignment of microtubules, focal contacts and actin filaments in fibroblasts spreading on smooth and grooved titanium substrata. *J. Cell Sci.* **106**, 343–354 (1993).
8. A. Mathur, S. W. Moore, M. P. Sheetz, J. Hone, The role of feature curvature in contact guidance. *Acta Biomater.* **8**, 2595–2601 (2012).
9. D. Franco *et al.*, Control of initial endothelial spreading by topographic activation of focal adhesion kinase. *Soft Matter* **7**, 7313–7324 (2011).
10. P. C. Wilkinson, J. M. Shields, W. S. Haston, Contact guidance of human neutrophil leukocytes. *Exp. Cell Res.* **140**, 55–62 (1982).
11. K. W. Kwon *et al.*, Nanotopography-guided migration of T cells. *J. Immunol.* **189**, 2266–2273 (2012).
12. M. K. Driscoll, X. Sun, C. Guven, J. T. Fourkas, W. Losert, Cellular contact guidance through dynamic sensing of nanotopography. *ACS Nano* **8**, 3546–3555 (2014).
13. X. Sun *et al.*, Asymmetric nanotopography biases cytoskeletal dynamics and promotes unidirectional cell guidance. *Proc. Natl. Acad. Sci. U.S.A.* **112**, 12557–12562 (2015).
14. A. Reversat *et al.*, Cellular locomotion using environmental topography. *Nature* **582**, 582–585 (2020).
15. V. Heinrich, C.-Y. Lee, Blurred line between chemotactic chase and phagocytic consumption: An immunophysical single-cell perspective. *J. Cell Sci.* **124**, 3041–3051 (2011).
16. V. Jaumouillé, A. X. Cartagena-Rivera, C. M. Waterman, Coupling of β₂ integrins to actin by a mechanosensitive molecular clutch drives complement receptor-mediated phagocytosis. *Nat. Cell Biol.* **21**, 1357–1369 (2019).
17. P. Rougerie, V. Miskolci, D. Cox, Generation of membrane structures during phagocytosis and chemotaxis of macrophages: Role and regulation of the actin cytoskeleton. *Immunol. Rev.* **256**, 222–239 (2013).
18. V. Jaumouillé, C. M. Waterman, Physical constraints and forces involved in phagocytosis. *Front. Immunol.* **11**, 1097 (2020).
19. J. A. Swanson, S. C. Baer, Phagocytosis by zippers and triggers. *Trends Cell Biol.* **5**, 89–93 (1995).
20. J. Mercer, A. Helenius, Vaccinia virus uses macropinocytosis and apoptotic mimicry to enter host cells. *Science* **320**, 531–535 (2008).
21. L. Mu *et al.*, A phosphatidylinositol 4,5-bisphosphate redistribution-based sensing mechanism initiates a phagocytosis programing. *Nat. Commun.* **9**, 4259 (2018).
22. R. M. Gilberti, D. A. Knecht, Macrophages phagocytose nonopsonized silica particles using a unique microtubule-dependent pathway. *Mol. Biol. Cell* **26**, 518–529 (2015).
23. P. Pacheco, D. White, T. Sulchek, Effects of microparticle size and Fc density on macrophage phagocytosis. *PLoS One* **8**, e60989 (2013).
24. M. Galic *et al.*, External push and internal pull forces recruit curvature-sensing N-BAR domain proteins to the plasma membrane. *Nat. Cell Biol.* **14**, 874–881 (2012).
25. W. Zhao *et al.*, Nanoscale manipulation of membrane curvature for probing endocytosis in live cells. *Nat. Nanotechnol.* **12**, 750–756 (2017).
26. H.-Y. Lou *et al.*, Membrane curvature underlies actin reorganization in response to nanoscale surface topography. *Proc. Natl. Acad. Sci. U.S.A.* **116**, 23143–23151 (2019).
27. O. Hoeller *et al.*, Two distinct functions for PI3-kinases in macropinocytosis. *J. Cell Sci.* **126**, 4296–4307 (2013).
28. A. T. Sasaki *et al.*, G protein-independent Ras/PI3K/F-actin circuit regulates basic cell motility. *J. Cell Biol.* **178**, 185–191 (2007).
29. D. Taniguchi *et al.*, Phase geometries of two-dimensional excitable waves govern self-organized morphodynamics of amoeboid cells. *Proc. Natl. Acad. Sci. U.S.A.* **110**, 5016–5021 (2013).
30. S. Fukushima, S. Matsuoka, M. Ueda, Excitable dynamics of Ras triggers spontaneous symmetry breaking of PIP3 signaling in motile cells. *J. Cell Sci.* **132**, jcs224121 (2019).
31. G. Gerisch *et al.*, Self-organizing actin waves as planar phagocytic cup structures. *Cell Adh. Migr.* **3**, 373–382 (2009).
32. D. M. Veltman *et al.*, A plasma membrane template for macropinocytic cups. *eLife* **5**, e20085 (2016).
33. G. Bloomfield *et al.*, Neurofibromin controls macropinocytosis and phagocytosis in *Dictyostelium*. *eLife* **4**, e04940 (2015).
34. T. D. Williams, R. R. Kay, The physiological regulation of macropinocytosis during *Dictyostelium* growth and development. *J. Cell Sci.* **131**, jcs213736 (2018).
35. M. Marinović *et al.*, IQGAP-related protein IqgC suppresses Ras signaling during large-scale endocytosis. *Proc. Natl. Acad. Sci. U.S.A.* **116**, 1289–1298 (2019).
36. C.-L. Chen, Y. Wang, H. Sesaki, M. Iijima, Myosin I links PIP3 signaling to remodeling of the actin cytoskeleton in chemotaxis. *Sci. Signal.* **5**, ra10 (2012).
37. G. Buczynski *et al.*, Inactivation of two *Dictyostelium discoideum* genes, DdPIK1 and DdPIK2, encoding proteins related to mammalian phosphatidylinositide 3-kinases, results in defects in endocytosis, lysosome to postlysosome transport, and actin cytoskeleton organization. *J. Cell Biol.* **136**, 1271–1286 (1997).
38. T. Bretschneider *et al.*, The three-dimensional dynamics of actin waves, a model of cytoskeletal self-organization. *Biophys. J.* **96**, 2888–2900 (2009).
39. T. A. Masters, M. P. Sheetz, N. C. Gauthier, F-actin waves, actin cortex disassembly and focal exocytosis driven by actin-phosphoinositide positive feedback. *Cytoskeleton* **73**, 180–196 (2016).
40. B. Schroth-Diez *et al.*, Propagating waves separate two states of actin organization in living cells. *HFSP J.* **3**, 412–427 (2009).

41. J. Helenius, M. Ecke, D. J. Müller, G. Gerisch, Oscillatory switches of dorso-ventral polarity in cells confined between two surfaces. *Biophys. J.* **115**, 150–162 (2018).

42. S. I. Gharbi *et al.*, Exploring the specificity of the PI3K family inhibitor LY294002. *Biochem. J.* **404**, 15–21 (2007).

43. S. Lee, J. W. Han, L. Leeper, J. S. Gruver, C. Y. Chung, Regulation of the formation and trafficking of vesicles from Golgi by PCH family proteins during chemotaxis. *Biochim. Biophys. Acta* **1793**, 1199–1209 (2009).

44. M. Yoshida, J. Stadler, G. Bertholdt, G. Gerisch, Wheat germ agglutinin binds to the contact site A glycoprotein of *Dictyostelium discoideum* and inhibits EDTA-stable cell adhesion. *EMBO J.* **3**, 2663–2670 (1984).

45. E. M. Reichl *et al.*, Interactions between myosin and actin crosslinkers control cytokinesis contractility dynamics and mechanics. *Curr. Biol.* **18**, 471–480 (2008).

46. Y.-S. Kee *et al.*, A mechanosensory system governs myosin II accumulation in dividing cells. *Mol. Biol. Cell* **23**, 1510–1523 (2012).

47. N. Saito, S. Sawai, Three-dimensional morphodynamics simulations of macropinocytic cups. *iScience* **24**, 103087 (2021).

48. T. Bretschneider *et al.*, Dynamic actin patterns and Arp2/3 assembly at the substrate-attached surface of motile cells. *Curr. Biol.* **14**, 1–10 (2004).

49. M. Jasnin *et al.*, The architecture of traveling actin waves revealed by cryo-electron tomography. *Structure* **27**, 1211–1223.e5 (2019).

50. Y. Miao *et al.*, Altering the threshold of an excitable signal transduction network changes cell migratory modes. *Nat. Cell Biol.* **19**, 329–340 (2017).

51. K. Takeda *et al.*, Incoherent feedforward control governs adaptation of activated Ras in a eukaryotic chemotaxis pathway. *Sci. Signal.* **5**, ra2 (2012).

52. A. Nakajima, S. Ishihara, D. Imoto, S. Sawai, Rectified directional sensing in long-range cell migration. *Nat. Commun.* **5**, 5367 (2014).

53. N. S. Gov, Guided by curvature: Shaping cells by coupling curved membrane proteins and cytoskeletal forces. *Philos. Trans. R. Soc. Lond. B Biol. Sci.* **373**, 20170115 (2018).

54. L. B. Case, C. M. Waterman, Adhesive F-actin waves: A novel integrin-mediated adhesion complex coupled to ventral actin polymerization. *PLoS One* **6**, e26631 (2011).

55. K. Plak, H. Pots, P. J. Van Haastert, A. Kortholt, Direct interaction between TalinB and Rap1 is necessary for adhesion of *Dictyostelium* cells. *BMC Cell Biol.* **17**, 1 (2016).

56. S. I. Yamazaki *et al.*, Talin B regulates collective cell migration via PI3K signaling in *Dictyostelium discoideum* mounds. *Biochem. Biophys. Res. Commun.* **525**, 372–377 (2020).

57. Y. Ren *et al.*, Mechanosensing through cooperative interactions between myosin II and the actin crosslinker cortexillin I. *Curr. Biol.* **19**, 1421–1428 (2009).

58. M. K. Pramanik, M. Iijima, Y. Iwadate, S. Yumura, PTEN is a mechanosensing signal transducer for myosin II localization in *Dictyostelium* cells. *Genes Cells* **14**, 821–834 (2009).

59. S. Lee, Z. Shen, D. N. Robinson, S. Briggs, R. A. Firtel, Involvement of the cytoskeleton in controlling leading-edge function during chemotaxis. *Mol. Biol. Cell* **21**, 1810–1824 (2010).

60. M. Jasnin, M. Ecke, W. Baumeister, G. Gerisch, Actin organization in cells responding to a perforated surface, revealed by live imaging and cryo-electron tomography. *Structure* **24**, 1031–1043 (2016).

61. D. Cox, C.-C. Tseng, G. Bjekic, S. Greenberg, A requirement for phosphatidylinositol 3-kinase in pseudopod extension. *J. Biol. Chem.* **274**, 1240–1247 (1999).

62. N. Araki, T. Hatae, A. Furukawa, J. A. Swanson, Phosphoinositide-3-kinase-independent contractile activities associated with Fcgamma-receptor-mediated phagocytosis and macropinocytosis in macrophages. *J. Cell Sci.* **116**, 247–257 (2003).

63. Y. Yang, D. Xiong, A. Pipathsouk, O. D. Weiner, M. Wu, Clathrin assembly defines the onset and geometry of cortical patterning. *Dev. Cell* **43**, 507–521.e4 (2017).

64. Z. Wu, M. Su, C. Tong, M. Wu, J. Liu, Membrane shape-mediated wave propagation of cortical protein dynamics. *Nat. Commun.* **9**, 136 (2018).

65. L. Pieuchot *et al.*, Curvotaxis directs cell migration through cell-scale curvature landscapes. *Nat. Commun.* **9**, 3995 (2018).

66. T. Chen *et al.*, Large-scale curvature sensing by directional actin flow drives cellular migration mode switching. *Nat. Phys.* **15**, 393–402 (2019).

67. N. D. Bade, R. D. Kamien, R. K. Assoian, K. J. Stebe, Curvature and Rho activation differentially control the alignment of cells and stress fibers. *Sci. Adv.* **3**, e1700150 (2017).

68. O. D. Weiner, W. A. Marganski, L. F. Wu, S. J. Altschuler, M. W. Kirschner, An actin-based wave generator organizes cell motility. *PLoS Biol.* **5**, e221 (2007).

69. H. Katsuno *et al.*, Actin migration driven by directional assembly and disassembly of membrane-anchored actin filaments. *Cell Rep.* **12**, 648–660 (2015).

70. Y. Asano, A. Nagasaki, T. Q. P. Uyeda, Correlated waves of actin filaments and PIP3 in *Dictyostelium* cells. *Cell Motil. Cytoskeleton* **65**, 923–934 (2008).

71. D. M. Veltman, M. G. Lemieux, D. A. Knecht, R. H. Insall, PIP$_3$-dependent macropinocytosis is incompatible with chemotaxis. *J. Cell Biol.* **204**, 497–505 (2014).

72. R. R. Kay, T. D. Williams, J. D. Manton, D. Traynor, P. Paschke, Living on soup: Macropinocytic feeding in amoebae. *Int. J. Dev. Biol.* **63**, 473–483 (2019).

73. V. P. Sharma *et al.*, Reconstitution of in vivo macrophage-tumor cell pairing and streaming motility on one-dimensional micro-patterned substrates. *Intravital* **1**, 77–85 (2012).

74. T. Fujimori, A. Nakajima, N. Shimada, S. Sawai, Tissue self-organization based on collective cell migration by contact activation of locomotion and chemotaxis. *Proc. Natl. Acad. Sci. U.S.A.* **116**, 4291–4296 (2019).

75. A. Nakajima, M. Ishida, T. Fujimori, Y. Wakamoto, S. Sawai, The microfluidic lighthouse: An omnidirectional gradient generator. *Lab Chip* **16**, 4382–4394 (2016).

76. G. A. Dunn, Characterising a kinesis response: Time averaged measures of cell speed and directional persistence. *Agents Actions Suppl.* **12**, 14–33 (1983).

Honda et al.
Microtopographical guidance of macropinocytic signaling patches

PNAS | 11 of 11
https://doi.org/10.1073/pnas.2110281118